



Cite this: *Phys. Chem. Chem. Phys.*,  
2019, 21, 1484

# A molecular dynamics study on the interface morphology of vapor-deposited amorphous organic thin films†

Dongsun Yoo,<sup>‡</sup><sup>a</sup> Hochul Song,<sup>‡</sup><sup>a</sup> Yong Youn,<sup>‡</sup><sup>a</sup> Sang Ho Jeon,<sup>b</sup> Youngmi Cho<sup>b</sup>  
and Seungwu Han<sup>\*a</sup>

The interfaces between amorphous organic layers play an important role in the efficiency and lifetime of organic light emitting diodes (OLEDs). However, an atomistic understanding of the interface morphology is still poor. In this study, we theoretically investigate the interfacial structure of amorphous organic films using molecular dynamics simulations that mimic vapor-deposition processes. We find that molecularly sharp interfaces are formed by the vapor-deposition process as the interface thickness spans only a mono- or double-layer in terms of lie-down geometry. Interestingly, the interface is more diffusive into the upper layer due to asymmetric interdiffusion during the vapor-deposition process, which is well described by a simple random-walk model. Additionally, we investigate the change in the molecular orientation of interdiffused molecules, which is crucial for device performance.

Received 20th August 2018,  
Accepted 17th December 2018

DOI: 10.1039/c8cp05294h

rsc.li/pccp

## 1 Introduction

Organic electronics have attracted considerable interest over the past two decades owing to several advantages such as low cost, flexibility, and variety of material libraries. In particular, significant advances were achieved in the applications of organic light-emitting diodes (OLEDs),<sup>1–4</sup> organic photovoltaics (OPVs),<sup>5–7</sup> and organic thin-film transistors (OTFTs).<sup>8,9</sup> In these devices, high efficiencies are achieved by employing multilayer structures.<sup>10,11</sup> For example, OLEDs incorporate multiple organic layers such as an electron transport layer, hole blocking layer, emissive layer, *etc.* In the multilayer structure, the interfaces between the layers play an important role in device efficiency and lifetime.<sup>12</sup> For instance, the performance of solution-processed OLEDs lags behind that of vapor-deposited OLEDs due to intermixing among the layers.<sup>13</sup> In OPVs, the interface morphology dictates the energy-level alignment and charge dynamics.<sup>14–19</sup> It was also reported that the organic film at elevated temperatures undergoes a phase transformation that propagates from the interface,<sup>20–23</sup> which implies that the interfacial structure is closely related to device stability and lifetime.

The above discussions underscore the importance of understanding and controlling the interface structures in improving the performance and lifetime of organic devices. Various experimental techniques such as secondary-ion mass spectroscopy,<sup>18,24</sup> neutron reflectometry,<sup>12,13,25</sup> X-ray scattering,<sup>14,26,27</sup> and photoelectron spectroscopy<sup>14,18,26,27</sup> have been employed to study the interfacial structures, but their resolution is not sufficient for revealing microscopic structures in full detail. Furthermore, the mixed interlayer that forms even at room temperature complicates the experimental characterization.<sup>14</sup>

With realistic interatomic interactions, molecular dynamics (MD) simulation has been a favored theoretical method for investigating the interfacial structures, which complements the experimental analysis. A multitude of MD simulations were carried out on the organic multilayers used in OPVs and OTFTs,<sup>15,16,28–34</sup> and they successfully linked the interface morphology such as molecular packing and orientation to the electronic properties like band alignment and charge dynamics.<sup>15,16,34</sup> However, most of these simulations involved a crystalline substrate for constructing the multilayers. In OLEDs, which is the main device that the present study is concerned with, every organic film is amorphous. In this case, one may simply cut and join two bulk amorphous phases to simulate the interface between the amorphous organic layers.<sup>31</sup> However, as was demonstrated for the single-layer film,<sup>35–37</sup> the deposition conditions significantly influence the molecular orientation in the vacuum-deposited organic films due to the limited diffusion of organic molecules, which in turn critically affects the device performance.<sup>14,38</sup> This implies that the deposition-based construction of the interface model is necessary.

<sup>a</sup> Department of Materials Science and Engineering and Research Institute of Advanced Materials, Seoul National University, Seoul 08826, Korea.

E-mail: hansw@snu.ac.kr

<sup>b</sup> Display R&D Center, Samsung Display Co., Ltd, 1 Samsung-ro, Giheung-gu, Yongin-si, Gyeonggi-do 17113, Korea

† Electronic supplementary information (ESI) available. See DOI: 10.1039/c8cp05294h

‡ These authors contributed equally.

As far as we are aware, such simulations have not been attempted yet.

In this study, using all-atom MD simulations of vapor-deposition processes, we model the organic–organic interfaces that exist in OLEDs and investigate the interface structure microscopically. In our previous study, we carried out MD simulations to obtain the process-dependent structure of a single organic layer.<sup>35</sup> Here, we extend this methodology to study the interface morphology. By analyzing the structure atomistically, we reveal the structural characteristics of vapor-deposited organic–organic interfaces and suggest the underlying formation mechanism. We also examine how the orientation of interdiffused molecules changes, which is crucial for the OLED performance.

## 2 Methods

### 2.1 Vapor-deposition simulation

The interfacial structure of vapor-deposited organic films is modeled by using all-atom molecular dynamics simulation that mimics the vapor-deposition process. The simulation method is based on that used in our previous study,<sup>35</sup> which well reproduced important features of experimental results. Among the organic molecules widely used in OLEDs, we choose three molecules considering the glass-transition temperature ( $T_g$ ), shape, and length; 4,4'-bis(*N*-carbazolyl)-1,1'-biphenyl (CBP), *N,N'*-diphenyl-*N,N'*-bis(1-naphthyl)-1,1'-biphenyl-4,4'-diamine ( $\alpha$ -NPD) and 4,4'-bis[*N*-carbazole]styryl]-biphenyl (BSB-Cz). The structural formulae of these molecules are given in Fig. 1 and additional information such as  $T_g$ , molecular length, and molecular volume is provided in the ESI.† The simulation is performed by using the LAMMPS<sup>39</sup> code with the all-atom optimized potential for liquid simulations (OPLS-AA)<sup>40,41</sup> force field. The default OPLS-AA parameters are used when available. The fitted parameters of a carbazole monomer<sup>42</sup> are used to describe the carbazolyl group. Since the conformation of  $\alpha$ -NPD is more complicated than other molecules, we fit some force-field parameters of  $\alpha$ -NPD to density-functional-theory (DFT) data. Atomic charges are evaluated from electrostatic-potential charges<sup>43</sup> and the main dihedral parameters are fitted to reproduce the potential energy surface of constrained

DFT calculations. For more details on fitting the force field parameters, we refer to the previous study.<sup>35</sup>

The deposition process is simulated by dropping a molecule into the simulation box every 250 ps with an initial velocity of 1–2 Å ps<sup>-1</sup> towards the C<sub>60</sub>(001) substrate. The bottom-most part is fixed, and the other parts are simulated using the *NVT* ensemble using the Nosé–Hoover thermostat with a time step of 1 fs. A cutoff distance of 10 Å is applied to the Coulomb and van der Waals interactions and the long-range electrostatic interactions are not considered (see ESI† for comparison). The deposition rates are 0.06–0.13 molecules nm<sup>-2</sup> ns<sup>-1</sup>, which are similar to the values obtained in other vapor-deposition simulations.<sup>29,44</sup> These deposition rates are much faster than those of the typical experimental conditions, meaning that the deposited molecules in the simulation box have much less time to diffuse. To compensate this time-scale gap, we accelerate the diffusion of the deposited molecules by maintaining the temperature of the last deposited molecule above  $T_g$ . Lyubimov *et al.*<sup>37</sup> showed that a high deposition rate causes a temperature shift while preserving the structural properties. Therefore, we expect that the present simulations are comparable to experiment except that the corresponding temperature would be lower in experiment. (The direct extrapolation to the experimental timescale is not feasible because of the high computational cost in obtaining multiple points and uncertainty in the extrapolation.) The *x* and *y* dimensions of the simulation box are set to be longer than three times the molecular length (8.4 nm for the system with BSB-Cz, and 5.6 nm for the CBP/ $\alpha$ -NPD system).

The interfacial structure is modeled by growing two layers sequentially. Each layer is deposited until its thickness reaches ~6 nm. The total simulation takes 6.6–13.3 × 10<sup>7</sup> steps, which corresponds to 66–133 ns. The final structures contain 650–1380 molecules in total. We consider four types of interfaces: CBP/BSB-Cz, BSB-Cz/CBP, CBP/ $\alpha$ -NPD, and  $\alpha$ -NPD/CBP. (A/B means that the B layer is grown on top of the A layer.) CBP/BSB-Cz is a typical interface between two linear molecules with different chain lengths, whereas CBP/ $\alpha$ -NPD may represent the interface between a linear molecule and a more three-dimensional molecule. The deposition process is simulated at two substrate temperatures (400 and 450 K) to study how the temperature affects the molecular orientation around the interface. Each temperature was chosen because organic molecules have distinct orientations in the bulk film.<sup>35</sup> Specifically, at 400 K, the average percentage of the horizontal component of the long molecular axis vector is 87% for CBP and 77% for NPD (the ratio is 67% for an isotropic film). At 450 K, the ratio is 93% for BSB-Cz and 63% for CBP, meaning that BSB-Cz tends to lie down and CBP is slightly standing up. Note that the substrate temperature does not correspond to the actual temperature in the experiment due to the limited diffusion time in the simulation.<sup>35</sup>

The molecular orientation of the deposited film is investigated using the orientational order parameter  $S$ , which is defined as

$$S = \frac{3\langle \cos^2 \theta \rangle - 1}{2}, \quad (1)$$

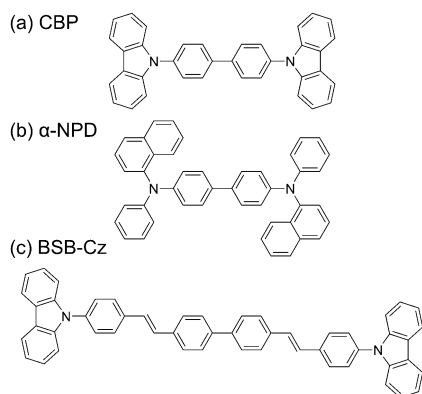


Fig. 1 Structural formulae of molecules used in the simulation.

where the angled bracket indicates the ensemble average and  $\theta$  is the angle between the molecular axis and the substrate normal. We define the molecular axis as an axis connecting two nitrogen atoms in each molecule. When every molecule is oriented horizontally, isotropically, and vertically,  $S$  equals  $-0.5$ ,  $0$ , and  $1$ , respectively. The ensemble average in eqn (1) is applied over the entire film. We note that the first few layers of the bottom layers are oriented more horizontally because they are close to the crystalline substrate, and thus they have smaller  $S$  values than in the bulk. However, their influence on the average  $S$  is negligible (within 0.01) because of their small fraction.

## 2.2 Frozen-bulk method

Modeling the interfacial structure requires simulations of a system that is much larger than a single-layer film, and the computational cost becomes prohibitively expensive as the film thickness increases during the deposition process. To overcome this, we introduce a technical approximation dubbed the “frozen-bulk method” that can significantly increase the computational speed without compromising the accuracy. The frozen-bulk method was inspired by the observation that if the temperature is lower than  $T_g$ , the morphology of the bulk region that is far away from the surface does not change meaningfully during the simulation. In addition, we confirmed that the local vibration within the bulk region does not affect the morphology of the upper layers (not shown). Therefore, one can fix the atomic positions in the bulk region and still obtain the same morphology.

Fig. 2 shows the idea of the frozen-bulk method schematically. The distance from the surface to the frozen bulk (‘Fixed’ in Fig. 2) is determined by inspecting the orientational change against depth during the simulation (see ESI† for details and validation). On the other hand, the thickness of the fixed region is chosen by considering the pairwise cutoff and molecular length. For instance, in the case of the BSB-Cz/CBP film in Fig. 2, the distance from the surface to the fixed region is 6 nm (about three times the molecular length) and the thickness of the fixed region is 2 nm. The region below the frozen bulk is removed from the simulation box for further speeding-up (‘Removed’ in Fig. 2).

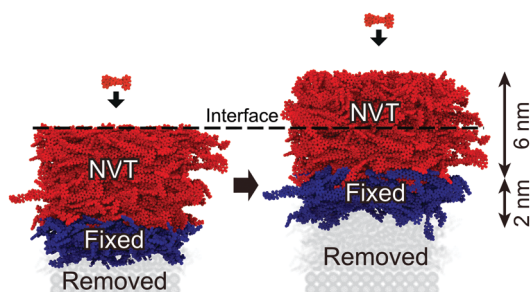


Fig. 2 Schematic figure describing the frozen-bulk method with an example of depositing CBP molecules on the BSB-Cz film. Red and blue molecules indicate *NVT* and fixed parts, respectively. The molecules removed from the simulation are coloured in grey. The interface between CBP and BSB-Cz is marked by the horizontal dashed line.

The regions are determined every time when a new molecule is deposited. After the deposition simulation is completed, the final structure is reconstructed by attaching the removed parts to the final snapshot. A further equilibration step is not performed because the structural changes were negligible when tested on the BSB-Cz/CBP sample (see ESI† for detailed validation). By utilizing the frozen-bulk method, we were able to accelerate the simulation by up to 5 times without sacrificing the accuracy. We note that the fixed part could affect the dynamics of adjacent molecules. However, since the thickness of the *NVT* part was carefully set to be sufficiently large, the influence of the fixed part on the results is negligible (see ESI† for validation).

## 2.3 Definition of interdiffusion

When two layers form an interface, the sharpness of the interface is important, which is related to the interdiffusion of the adjacent layers. The degree of interdiffusion is usually estimated by the density profile of each component along the normal direction of the interface. However, when the intermixed layer is as thin as a few nanometers, such a plane-average method becomes less reliable because of lateral roughness in the density profile. In the present work, we introduce a more microscopic definition for interdiffusion. First, we define a set of atoms,  $N(m)$ , that neighbors a certain molecule  $m$  within the specific cutoff distance ( $r_c$ ; 6 Å in the present work). That is to say, atoms belonging to  $N(m)$  are within  $r_c$  of a certain atom in molecule  $m$  (but not a part of  $m$ ). Fig. 3 shows the definition of  $N(m)$  schematically. Physically, the atoms in  $N(m)$  are those effectively interacting with the molecule  $m$ , and this definition allows for the consideration of a non-spherical molecular shape as well.

Based on  $N(m)$ , we define  $P(m;A)$  as the proportion of A-type molecules among the neighbors of molecule  $m$ :

$$P(m;A) = \frac{\sum_{j \in N(m)} [t_j = A]}{\sum_{j \in N(m)} 1}, \quad (2)$$

where the square-bracket function in the numerator is 1 if the type of molecule containing atom  $j$  ( $t_j$ ) is A, and zero otherwise.

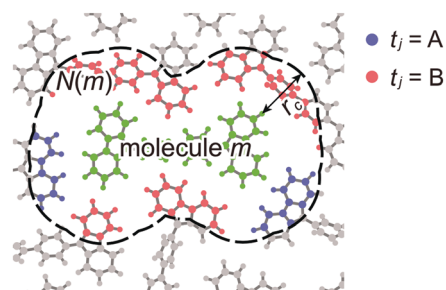


Fig. 3 Schematic figure showing the definition of  $N(m)$ . Green points are atoms that belong to the molecule of interest (molecule  $m$ ). Blue and red points within the dashed boundary are atoms in the molecule of type A and B, respectively, that are within the cutoff radius ( $r_c$ ) from a certain atom in molecule  $m$ .  $N(m)$  is the set of blue and red points.

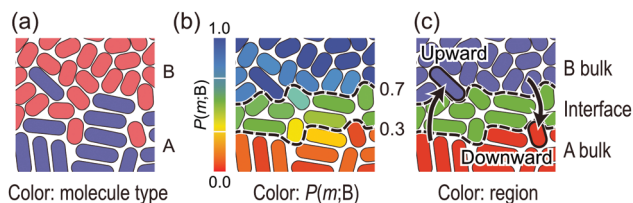


Fig. 4 Schematic illustration of the A/B interface colored with (a) molecule type, (b)  $P(m;B)$ , and (c) distinct regions. The dashed lines in (b) and (c) are the contour lines on which  $P(m;B)$  is 0.3 or 0.7. The interdiffused molecules are highlighted in (c) by arrows.

Now, we divide the A/B multilayer into three distinct regions according to the value of  $P(m;A)$ :

$$\text{Region} = \begin{cases} \text{bulk of A} & \text{if } P(m;A) > 0.5 + P_{\text{th}} \\ \text{bulk of B} & \text{if } P(m;A) < 0.5 - P_{\text{th}} \\ \text{interface} & \text{otherwise} \end{cases} \quad (3)$$

This regional division facilitates analysis on the interface structure and quantification of interdiffusion. In eqn (3), the threshold value  $P_{\text{th}}$  is set to 0.2, but the results are largely insensitive to the choice of  $P_{\text{th}}$ . Finally, we define interdiffusion in the A/B multi-layer as the diffusion of A molecules into the bulk region of B (upward-diffusion) or *vice versa* (downward-diffusion). Fig. 4 illustrates these definitions.

### 3 Results and discussion

Using the methods outlined in the previous section, we carried out MD simulations and obtained interfacial structures with the four combinations. For the statistical average, we repeated the simulation three and four times for each interface model containing  $\alpha$ -NPD and BSB-Cz molecules, respectively. The total numbers of molecules involved in the average are 130–284 (148–356) for the interface region and 2–14 (4–33) for the interdiffused molecules at 400 K (450 K). As a representative case, Fig. 5 shows the structure of the BSB-Cz/CBP film obtained from the MD simulations. For visual clarity, the CBP

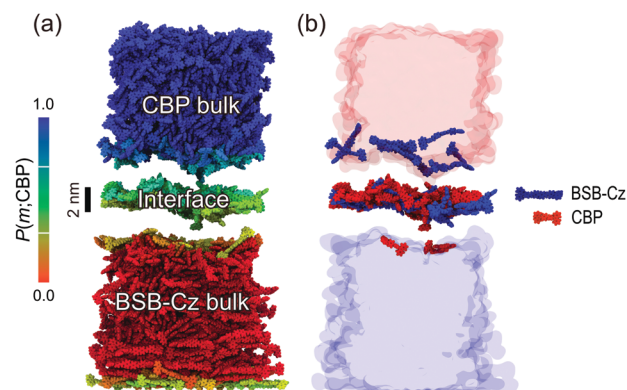


Fig. 5 The structure of the BSB-Cz/CBP film that is split apart according to the region. Molecules are colored by (a) their  $P(m;CBP)$  values and (b) their types. In (b), molecules in the bulk region are rendered transparent.

and BSB-Cz bulk regions identified by eqn (3) are artificially pulled apart.

The interface thickness is typically estimated from the  $xy$ -averaged density profile of each component along the  $z$ -axis (substrate normal). However, this plane-average method can overestimate the interface thickness because the interface roughness smears the density profile. Here, we propose a new method to estimate the interface thickness based on the region defined in eqn (3). The interface thickness can be calculated by first dividing the  $xy$ -plane into  $4 \times 4 \text{ \AA}^2$  grids and then calculating the thickness of each grid as the difference between the maximum and minimum  $z$ -coordinates of the molecular surface of the interface region within the grid. The molecular surface is constructed by convoluting the atomic sphere of the van der Waals radius with the atomic positions. The average of the grid thickness is regarded as the interface thickness. The density profile along the vertical direction and the comparison between the interface thicknesses evaluated by the plane-average method and the new method are given in the ESI.† We note from the density profile that the interface region is densely packed and the molecular mixing in the interface region does not give rise to a low-density region.

The average thickness of each interface type is compiled in Table 1. Several observations can be noted; the interface thickness spans around 1–2 molecular layers (in lie-down geometry), which is much sharper than the solution-processed films, whose thickness is typically 10–20 nm.<sup>12,24</sup> On average, the thickness increases by 27% when the substrate temperature increases from 400 to 450 K, which is a result of the enhanced thermal diffusion. The difference in the interface thickness between A/B and B/A (reversed deposition order) is 3% on average, suggesting that the deposition order has little influence on the interface thickness. It is also notable that the interface thickness increases by 15% when BSB-Cz is replaced with  $\alpha$ -NPD although the degree of interdiffusion is similar (see Fig. 6).

In Fig. 5b, the molecules are colored by their type, which identifies the interdiffused molecules in the opposite bulk regions. This can be quantitatively analyzed in terms of interdiffused volume that is defined as the number of interdiffused molecules multiplied by their molecular volume in the bulk amorphous phase. Fig. 6 shows the total interdiffused volume per area for the four interface types. It can be seen that the upward-diffusion is more frequent than the downward-diffusion in all samples (on average 2.5 times), which implies that the interface morphology is asymmetric. The detailed explanation will be given below. It can also be seen that the interdiffusion is significantly enhanced at higher temperatures.

Characteristic features in Fig. 6 can be understood by tracing atomic trajectories during MD simulations. For example, it can be found from the 450 K data that the diffusion direction is

Table 1 Average thickness (Å) of interface layer

|       | CBP/BSB-Cz | BSB-Cz/CBP | CBP/ $\alpha$ -NPD | $\alpha$ -NPD/CBP |
|-------|------------|------------|--------------------|-------------------|
| 400 K | 8.38       | 9.33       | 10.38              | 10.67             |
| 450 K | 11.72      | 11.02      | 12.20              | 12.86             |

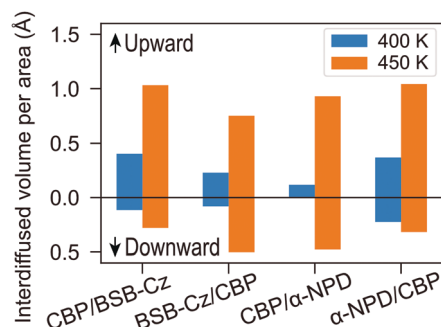


Fig. 6 Total interdiffused volume per area of the four interface types deposited at 400 and 450 K. The upper and lower parts show upward-diffusion and downward-diffusion, respectively.

more symmetric in BSB-Cz/CBP than in CBP/BSB-Cz. (This is less clear in the 400 K data because of the small sample size.) This is because CBP is more mobile than BSB-Cz due to the smaller molecular mass and shorter chain length. Even though upward-diffusion is more frequent in general (see below) and the molecular volume of BSB-Cz is 42% larger than that of CBP, the upward-diffusing BSB-Cz is slower than the downward-diffusing CBP in BSB-Cz/CBP, and so the asymmetry is partly suppressed. For another example, when comparing BSB-Cz/CBP to  $\alpha$ -NPD/CBP, it can be seen that  $\alpha$ -NPD is faster than BSB-Cz, which is expected from the difference in  $T_g$  between the two molecules. Besides  $T_g$ , the molecular shape also affects the interdiffusion; comparing BSB-Cz/CBP and  $\alpha$ -NPD/CBP, we note that the diffusion of CBP into  $\alpha$ -NPD is slower than the diffusion of CBP into BSB-Cz even though BSB-Cz has a higher  $T_g$ . Since  $\alpha$ -NPD molecules are interlocked due to the propeller-shaped side groups, it is difficult for CBP to penetrate and hence the diffusion of CBP into  $\alpha$ -NPD is hindered. In contrast, BSB-Cz and CBP both form stacked structures, which makes it easier for CBP to penetrate BSB-Cz by slipping.

The asymmetry between the upward-diffusion and downward-diffusion originates from the fundamental aspect of vapor-deposition processes, which applies to the single-layer as well as multi-layer. That is to say, the molecules near the surface have much higher mobility than the molecules in the bulk region because they are exposed to the free space. As such, one can simply consider the surface layer as mobile and the bulk layer as immobile. During the deposition process, the surface rises up and the molecules beneath the surface become immobile. Therefore, the molecules diffusing downward become immobile whereas the molecules diffusing upward remain mobile and so can diffuse further upward (see Fig. 7a). This asymmetric interdiffusion results in the interface morphology that is more diffusive into the upper layer. In contrast to asymmetric vertical distribution, we find that the lateral distribution of the molecules is random and uniform; no phase separation is observed, and the two types of molecules are evenly mixed like a solid solution.

To analyze the asymmetric interdiffusion quantitatively, we define the  $z$ -displacement as the displacement of the center of mass of a molecule in the  $z$ -direction in reference to the initial

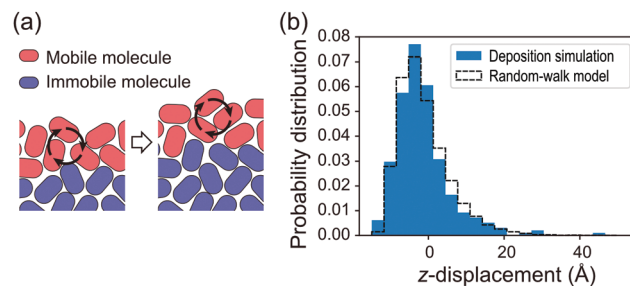


Fig. 7 (a) Schematic illustration of the diffusion during the vapor-deposition process. The molecules near the surface (red) are mobile whereas the molecules in the bulk (blue) are immobile. As the deposition progresses, the surface shifts upwards and so does the mobile region. While the mobile molecules that diffused downward become immobile, the molecules that diffused upward are still mobile. (b) The histogram of the displacement in the  $z$ -direction obtained from the deposition simulation of a CBP film and the random-walk model.

landing position on the surface. Therefore, a positive (negative)  $z$ -displacement means that the molecule diffused upward (downward) during the simulation. Fig. 7b shows the distribution of the  $z$ -displacement obtained from the deposition simulation of a pure CBP film. The distribution is positively skewed, meaning that the upward-diffusion is more active than the downward-diffusion. The distribution of  $z$ -displacement can also be reproduced by a simple one-dimensional random-walk model. In short, this model captures the key feature of the deposition process that the molecules are mobile within a certain surface thickness and stuck below this area. (The details of the model and simulation methods are provided in the ESI.†) With parameters adjusted properly, the model well reproduces the  $z$ -displacement of the CBP film, as shown by the dashed line in Fig. 7b.

Lastly, we investigate the molecular orientation since it is related to key properties such as charge transport and out-coupling efficiency in OLEDs.<sup>38</sup> (In OPVs and OTFTs, the molecular orientation at the interface affects the band alignment and charge transport.<sup>15–19</sup>) The molecular orientation is quantified by the orientational order parameter  $S$  as explained in the method section. Fig. 8 shows the region-averaged  $S$  values of the four interfaces deposited at 400 K and 450 K. We note that only a few molecules are intermixed at 400 K (see Fig. 6) and so the  $S$  values in those cases may not be statistically reliable for interdiffused molecules (these data are marked with empty symbols).

In Fig. 8, we notice that the molecular orientation in the interface region is similar to that in the bulk region in all cases; the intermixing does not lead to a dramatic change in the molecular orientation in the interface region. On the other hand, the films deposited at 450 K show that the  $S$  value of interdiffused molecules deviates from the value in the bulk region. To be specific, in the CBP/BSB-Cz and BSB-Cz/CBP films, the  $S$  value of interdiffused molecules becomes much closer to that of the other molecular species in their bulk region (except for the interdiffused BSB-Cz in the CBP). This can be explained in a similar way to the  $S$  value of a dopant in a host-dopant system that becomes closer to that of the host;<sup>35</sup>

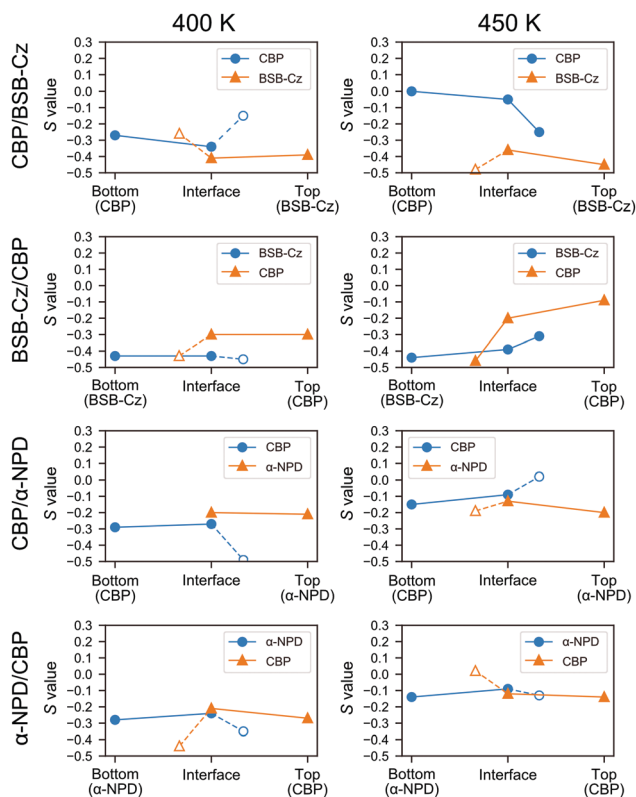


Fig. 8 Region-averaged orientational order parameter  $S$  in the four interface models. Blue (orange) dots indicate the  $S$  values of molecular species of the bottom (top) layer. The  $x$ -axis is divided into the bulk of the bottom layer, interface, and bulk of the top layer as defined in eqn (3). The  $S$  values of interdiffused molecules are plotted at the interface. The  $S$  values are indicated by empty symbols when the uncertainty is greater than  $\sim 0.2$  (estimated by the bias-corrected and accelerated (BCa) bootstrapping method).

since CBP, BSB-Cz, and  $\alpha$ -NPD do not have a permanent dipole moment, it is reasonable to assume that the molecular orientation is mainly determined by short-range interactions. Therefore, molecule  $m$  behaves as if it were embedded in an A-B mixture where the concentration of A is  $P(m;A)$ . We also note in Fig. 8 that the  $S$  value of CBP in the interface region of CBP/BSB-Cz is higher than that of BSB-Cz/CBP since the proportion of the bottom-layer molecule at the interface is higher than that of the top-layer molecule. This indicates that the order of deposition affects the molecular orientation at the interface.

At 450 K, CBP and  $\alpha$ -NPD have similar  $S$  values. Therefore, the  $S$  values in the interface regions of  $\alpha$ -NPD/CBP and CBP/ $\alpha$ -NPD are almost the same as those in the bulk region. However, it is noticeable that the interdiffused CBP has  $S$  values closer to zero in both  $\alpha$ -NPD/CBP and CBP/ $\alpha$ -NPD. This might be caused by the difference in the molecular shape between CBP and  $\alpha$ -NPD; BSB-Cz and CBP are both linear molecules, so they tend to align themselves, which biases the dopant molecules in the same direction. However, due to the propeller-shaped side groups in  $\alpha$ -NPD, the molecular axis of CBP may not easily align with that of  $\alpha$ -NPD even though they are close to each other. This suggests that planar molecules have a tendency of

having a random orientation when diffused into the bulk region of three-dimensional molecules.

## 4 Conclusions

In summary, we modeled the interfacial structure of amorphous organic multi-layers by molecular dynamics simulation that mimics the vapor-deposition process. We introduced the frozen-bulk method that speeds up the interface modeling, which allows for atomistic modeling of large stacks of organic layers. The interfacial structures were analyzed systematically by introducing  $P(m;A)$  that effectively represents the composition in the local environment. It was found that the thickness of the intermixed layer is about 1–2 molecular layers after simulations. The interfacial thickness depends on the substrate temperature and on the combination of compounds but little on the deposition order. The interface region was densely packed, and the molecules were evenly mixed like a solid solution. There was an asymmetry in the interdiffusion such that the upward-diffusion was stronger than the downward-diffusion. This was due to the asymmetric nature of the vapor-deposition process, which can be well described by the simple random-walk model. This asymmetric interdiffusion resulted in the interface morphology that is asymmetric in the vertical direction. The molecular orientation of interdiffused molecules was also investigated and it was found that when the orientation in the interface region was similar to that in the bulk region, the interdiffused molecules oriented as if they were in a host–dopant system.<sup>35</sup> The deposition order affected the molecular orientation in the interface region and the interdiffusion asymmetry.

The detailed knowledge of the density profile and molecular orientation obtained in this work will be useful for multi-scale device simulations to model more realistic interface structures,<sup>45</sup> which could predict the influence of the interface morphology on device performance. For instance, intermixing at the interface is known to both adversely and beneficially affect the device performance by increasing driving voltage,<sup>13</sup> suppressing charge accumulation,<sup>13</sup> and promoting charge separation.<sup>14</sup> Although this study focused on amorphous materials, the same modeling technique can be applied to interfaces including crystalline materials, which are used in OPVs and OTFTs. We believe that this study contributes to the understanding of the interface morphology and interface physics of organic thin films.

## Conflicts of interest

There are no conflicts to declare.

## Acknowledgements

This research was supported by Samsung Display and the Technology Innovation Program (or the Industrial Strategic Technology Development Program [10052925, Atomistic process and device modeling of sub-10 nm scale transistors]) funded

by the Ministry of Trade, Industry & Energy (MOTIE, Korea). The computations were performed at the KISTI supercomputing center (Grant No. KSC-2018-C3-0022).

## Notes and references

- 1 M. A. Baldo, S. Lamansky, P. E. Burrows, M. E. Thompson and S. R. Forrest, *Appl. Phys. Lett.*, 1999, **75**, 4–6.
- 2 S. Reineke, F. Lindner, G. Schwartz, N. Seidler, K. Walzer, B. Lüssem and K. Leo, *Nature*, 2009, **459**, 234–238.
- 3 B. W. D'Andrade and S. R. Forrest, *Adv. Mater.*, 2004, **16**, 1585–1595.
- 4 A. P. Kulkarni, C. J. Tonzola, A. Babel and S. A. Jenekhe, *Chem. Mater.*, 2004, **16**, 4556–4573.
- 5 L. Schmidt-Mende, A. Fechtenkötter, K. Müllen, E. Moons, R. H. Friend and J. D. MacKenzie, *Science*, 2001, **293**, 1119–1122.
- 6 Y. Sun, G. C. Welch, W. L. Leong, C. J. Takacs, G. C. Bazan and A. J. Heeger, *Nat. Mater.*, 2012, **11**, 44–48.
- 7 J.-H. Kim, E.-K. Park, J.-H. Kim, H. J. Cho, D.-H. Lee and Y.-S. Kim, *Electron. Mater. Lett.*, 2016, **12**, 383–387.
- 8 G. Giri, E. Verploegen, S. C. B. Mannsfeld, S. Atahan-Evrenk, D. H. Kim, S. Y. Lee, H. A. Becerril, A. Aspuru-Guzik, M. F. Toney and Z. Bao, *Nature*, 2011, **480**, 504–508.
- 9 C. Kim, A. Facchetti and T. J. Marks, *Science*, 2007, **318**, 76–80.
- 10 J. Kido, M. Kimura and K. Nagai, *Science*, 1995, **267**, 1332–1334.
- 11 C. W. Tang, *Appl. Phys. Lett.*, 1986, **48**, 183–185.
- 12 S. Ohisa, Y.-J. Pu, N. L. Yamada, G. Matsuba and J. Kido, *ACS Appl. Mater. Interfaces*, 2015, **7**, 20779–20785.
- 13 S. Ohisa, Y.-J. Pu, N. L. Yamada, G. Matsuba and J. Kido, *Nanoscale*, 2017, **9**, 25–30.
- 14 G. O. Ngongang Ndjawa, K. R. Graham, R. Li, S. M. Conron, P. Erwin, K. W. Chou, G. F. Burkhard, K. Zhao, E. T. Hoke, M. E. Thompson, M. D. McGehee and A. Amassian, *Chem. Mater.*, 2015, **27**, 5597–5604.
- 15 F. Castet, G. D'Avino, L. Muccioli, J. Cornil and D. Beljonne, *Phys. Chem. Chem. Phys.*, 2014, **16**, 20279–20290.
- 16 Y. T. Fu, D. A. Da Silva Filho, G. Sini, A. M. Asiri, S. G. Aziz, C. Risko and J. L. Brédas, *Adv. Funct. Mater.*, 2014, **24**, 3790–3798.
- 17 S. Verlaak, D. Beljonne, D. Cheyons, C. Rolin, M. Linares, F. Castet, J. Cornil and P. Heremans, *Adv. Funct. Mater.*, 2009, **19**, 3809–3814.
- 18 N. Sai, R. Gearba, A. Dolocan, J. R. Tritsch, W. L. Chan, J. R. Chelikowsky, K. Leung and X. Zhu, *J. Phys. Chem. Lett.*, 2012, **3**, 2173–2177.
- 19 C. Poelking, M. Tietze, C. Elschner, S. Olthof, D. Hertel, B. Baumeier, F. Würthner, K. Meerholz, K. Leo and D. Andrienko, *Nat. Mater.*, 2015, **14**, 434–439.
- 20 M. Tyliniski, A. Sepúlveda, D. M. Walters, Y. Z. Chua, C. Schick and M. D. Ediger, *J. Chem. Phys.*, 2015, **143**, 244509.
- 21 C. Rodríguez-Tinoco, M. Gonzalez-Silveira, J. Ràfols-Ribé, A. F. Lopeandía and J. Rodríguez-Viejo, *Phys. Chem. Chem. Phys.*, 2015, **17**, 31195–31201.
- 22 D. M. Walters, R. Richert and M. D. Ediger, *J. Chem. Phys.*, 2015, **142**, 134504.
- 23 S. S. Dalal and M. D. Ediger, *J. Phys. Chem. B*, 2015, **119**, 3875–3882.
- 24 N. Aizawa, Y.-J. Pu, M. Watanabe, T. Chiba, K. Ideta, N. Toyota, M. Igarashi, Y. Suzuri, H. Sasabe and J. Kido, *Nat. Commun.*, 2014, **5**, 5756.
- 25 A. J. Clulow, C. Tao, K. H. Lee, M. Velusamy, J. A. McEwan, P. E. Shaw, N. L. Yamada, M. James, P. L. Burn, I. R. Gentle and P. Meredith, *Langmuir*, 2014, **30**, 11474–11484.
- 26 J. D. Zimmerman, X. Xiao, C. K. Renshaw, S. Wang, V. V. Diev, M. E. Thompson and S. R. Forrest, *Nano Lett.*, 2012, **12**, 4366–4371.
- 27 U. Hörmann, C. Lorch, A. Hinderhofer, A. Gerlach, M. Gruber, J. Kraus, B. Sykora, S. Grob, T. Linderl, A. Wilke, A. Opitz, R. Hansson, A. S. Anselmo, Y. Ozawa, Y. Nakayama, H. Ishii, N. Koch, E. Moons, F. Schreiber and W. Brütting, *J. Phys. Chem. C*, 2014, **118**, 26462–26470.
- 28 Y. T. Fu, C. Risko and J. L. Brédas, *Adv. Mater.*, 2013, **25**, 878–882.
- 29 L. Muccioli, G. D'Avino and C. Zannoni, *Adv. Mater.*, 2011, **23**, 4532–4536.
- 30 G. Han, X. Shen and Y. Yi, *Adv. Mater. Interfaces*, 2015, **2**, 1500329.
- 31 R. Bhowmik, R. J. Berry, V. Varshney, M. F. Durstock and B. J. Leever, *J. Phys. Chem. C*, 2015, **119**, 27909–27918.
- 32 N. G. Martinelli, M. Savini, L. Muccioli, Y. Olivier, F. Castet, C. Zannoni, D. Beljonne and J. Cornil, *Adv. Funct. Mater.*, 2009, **19**, 3254–3261.
- 33 G. D'Avino, L. Muccioli and C. Zannoni, *Adv. Funct. Mater.*, 2015, **25**, 1985–1995.
- 34 T. Liu, D. L. Cheung and A. Troisi, *Phys. Chem. Chem. Phys.*, 2011, **13**, 21461.
- 35 Y. Youn, D. Yoo, H. Song, Y. Kang, K. Y. Kim, S. H. Jeon, Y. Cho, K. Chae and S. Han, *J. Mater. Chem. C*, 2018, **6**, 1015–1022.
- 36 S. S. Dalal, D. M. Walters, I. Lyubimov, J. J. de Pablo and M. D. Ediger, *Proc. Natl. Acad. Sci. U. S. A.*, 2015, **112**, 4227–4232.
- 37 I. Lyubimov, L. Antony, D. M. Walters, D. Rodney, M. D. Ediger and J. J. de Pablo, *J. Chem. Phys.*, 2015, **143**, 094502.
- 38 D. Yokoyama, *J. Mater. Chem.*, 2011, **21**, 19187–19202.
- 39 S. Plimpton, *J. Comput. Phys.*, 1995, **117**, 1–19.
- 40 W. L. Jorgensen, D. S. Maxwell and J. Tirado-Rives, *J. Am. Chem. Soc.*, 1996, **118**, 11225–11236.
- 41 G. A. Kaminski, R. A. Friesner, J. Tirado-Rives and W. L. Jorgensen, *J. Phys. Chem. B*, 2001, **105**, 6474–6487.
- 42 T. Vehoff, J. Kirkpatrick, K. Kremer and D. Andrienko, *Phys. Status Solidi B*, 2008, **245**, 839–843.
- 43 U. C. Singh and P. A. Kollman, *J. Comput. Chem.*, 1984, **5**, 129–145.
- 44 L. W. Antony, N. E. Jackson, I. Lyubimov, V. Vishwanath, M. D. Ediger and J. J. de Pablo, *ACS Cent. Sci.*, 2017, **3**, 415–424.
- 45 P. Kordt, J. J. M. van der Holst, M. Al Helwi, W. Kowalsky, F. May, A. Badinski, C. Lennartz and D. Andrienko, *Adv. Funct. Mater.*, 2015, **25**, 1955–1971.